arXiv:1703.10035v1 [cond-mat.mtrl-sci] 29 Mar 2017

# Identification of phase components in Zr-Ni and Hf-Ni intermetallic compounds; Investigations by perturbed angular correlation spectroscopy and first principles calculations

S.K. Dey[1,2], C.C. Dey[1,2*], S. Saha[1,2], J. Belošević-Čavor[3], D. Toprek[3]

[1] *Saha Institute of Nuclear Physics, 1/AF Bidhannagar, Kolkata-700 064, India*

[2] *Homi Bhabha National Institute, Anushaktinagar, Mumbai-400 094, India*

[3] *Institute of Nuclear Sciences Vinca, University of Belgrade, P. O. Box 522, 11001 Belgrade, Serbia*

**Abstract**

Time-differential perturbed angular correlation (TDPAC) measurements have been carried out in stoichiometric $ZrNi_3$ and $HfNi_3$ intermetallic compounds using $^{181}$Ta probe in the temperature range 77-1073 K considering the immense technological applications of Zr-Ni and Hf-Ni intermetallic compounds. In $ZrNi_3$, four components due to the production of $Zr_2Ni_7$, $Zr_8Ni_{21}$, $Zr_7Ni_{10}$ and $ZrNi_3$ have been found at room temperature. The $HfNi_3$ sample produces five electric quadrupole interaction frequencies at room temperature. The phase $HfNi_3$ is strongly produced in stoichiometric sample of $HfNi_3$ where two non-equivalent Hf sites are found to be present. Besides this phase, two other phases due to $Hf_2Ni_7$ and $Hf_8Ni_{21}$ have been found but, we do not observe any phase due to $Hf_7Ni_{10}$. X-ray diffraction and TEM/energy dispersive X-ray spectroscopy (EDX) measurements were used to further characterize the investigated materials and it was found that these results agree with the TDPAC results. In order to confirm findings from TDPAC measurements, density functional theory (DFT) based calculations of electric field gradients (EFG) and asymmetry parameters at the sites of $^{181}$Ta probe nucleus were performed. Our calculated results are found to be in excellent agreement with the experimental results.

*Keywords:* A. hydrogen absorbing materials; A. intermetallics; B. mechanical alloying; C. hyperfine interactions; D. perturbed angular correlations, PAC; D. X-ray diffraction;

## 1. Introduction

The elements zirconium and hafnium are alloyed with cobalt, nickel, titanium, palladium etc. to form many intermetallic compounds which have technological applications. Zirconium-nickel alloys are found to have useful hydrogen storage properties. It was shown that the compounds $Zr_8Ni_{21}$, $Zr_9Ni_{11}$, $Zr_7Ni_{10}$, $Zr_2Ni_7$, ZrNi are good hydrogen absorbing materials to form interstitial metal

*corresponding author

*Email addresses:* skumar.dey@saha.ac.in (S.K. Dey[1,2]), chandicharan.dey@saha.ac.in (C.C. Dey[1,2]), satyajit.saha@saha.ac.in (S. Saha[1,2]), cjeca@vin.bg.ac.rs (J. Belošević-Čavor[3]), toprek@vin.bg.ac.rs (D. Toprek[3])

hydrides (MH) which have important application in nickel metal hydride (NiMH) batteries as negative electrode material. The electrochemical properties of several Zr-Ni intermetallic compounds were studied earlier [1–6] by different workers. In $ZrNi_3$, catalytic hydrogen activity was reported by Wright et al. [7]. The hafnium alloyed with nickel, niobium, and tantalum are also useful and can withstand high temperature and pressure. Hafnium alloys are useful in medical implants and devices due to their bio-compatibility and corrosion resistance [8]. The alloys of Ni-Ti-Hf exhibit shape memory behavior [9]. Intermetallic compounds of Hf and transition metals (Fe, Co, Pd, Pt) have also hydrogen storage properties [10], with high H/M ratio at room temperature.

Time differential perturbed angular correlation (TDPAC) or simply PAC is an important nuclear technique to study the structural properties of compounds that contain hafnium and zirconium. Effects of a $\gamma$-$\gamma$ angular correlation in a crystalline environment are measured by this technique through hyperfine interaction (electric quadrupole and/or magnetic dipole). In electric quadrupole interaction, the quadrupole moment of the probe nucleus interacts with the electric field gradient (EFG) that arises in a crystalline material with noncubic symmetry due to charge distribution of the probe environment. In magnetic interaction, the magnetic dipole moment of the probe nucleus interacts with the internal/external magnetic field. Using this technique, several studies in Hf/Zr-Ni systems were carried out earlier to investigate their EFGs and magnetic properties [11–17]. Recently we have studied the structural properties of $(Zr/Hf)_8Ni_{21}$, $(Zr/Hf)_7Ni_{10}$ using the PAC technique [18, 19]. However, we do not find any previous PAC studies in $(Zr/Hf)Ni_3$. In the present report, attempts have been made to produce the intermetallic compounds $(Zr/Hf)Ni_3$ by arc melting of the constituent elements taken in stoichiometric ratios and characterize them by PAC spectroscopy. According to Becle et al. [20], the $ZrNi_3$ was formed from $Zr_2Ni_5$ and $Zr_2Ni_7$ at 940 °C or below by a peritectoid reaction. The stable phase of $ZrNi_3$ was obtained at room temperature by annealing the sample at ∼860 °C. They found that the phase $ZrNi_3$ was not stable and decayed at 940 °C following $4ZrNi_3 \rightarrow Zr_2Ni_7 + Zr_2Ni_5$. The phase $ZrNi_3$, however, was not found by other workers [21–23]. J. H. N. Van Vucht [24] also failed to produce $ZrNi_3$ by replacing Ti with Zr in $TiNi_3$. In order to help identifying the different phases produced in the investigated samples, the electric field gradients were calculated by density functional theory (DFT) and compared with the measured EFGs. The temperature dependent PAC measurements enabled us to find any structural changes in the material and give information on the structural stability of the compound.

The $ZrNi_3$ is known to be a hexagonal close-packed compound of the $SnNi_3$ type with space group $P6_3/mmc$. The lattice parameters were reported to be $a$=5.309 $\AA$ and $c$=4.303 $\AA$ [20]. Crystal structure of $HfNi_3$ was also reported by L. Bsenko [25]. It was found [25] that $HfNi_3$ exists in two modifications. A high temperature $\alpha$-$HfNi_3$ phase and a low temperature $\beta$-$HfNi_3$ phase. The crystal parameters for the two phases were reported to be $a$=5.27 $\AA$, $c$=19.2324 $\AA$ and $a$=5.2822 $\AA$, $c$=21.3916 $\AA$ for the $\alpha$ and $\beta$ phases, respectively.

## 2. Experimental details

To produce the intermetallic compounds $ZrNi_3$ and $HfNi_3$, stoichiometric amounts of constituent elements procured from M/S Alfa Aesar were taken. The purity of the metals used were : Zr-99.2% (excluding Hf), Hf-99.95%(excluding Zr) and Ni-99.98%. To introduce the $^{181}$Hf probe, each sample was remelted by adding an active piece of Hf wire (∼1 mg). Shiny globule samples were formed after melting in the arc furnace. Natural Hf (∼ 30% $^{180}$Hf) was pre-activated to $^{181}$Hf

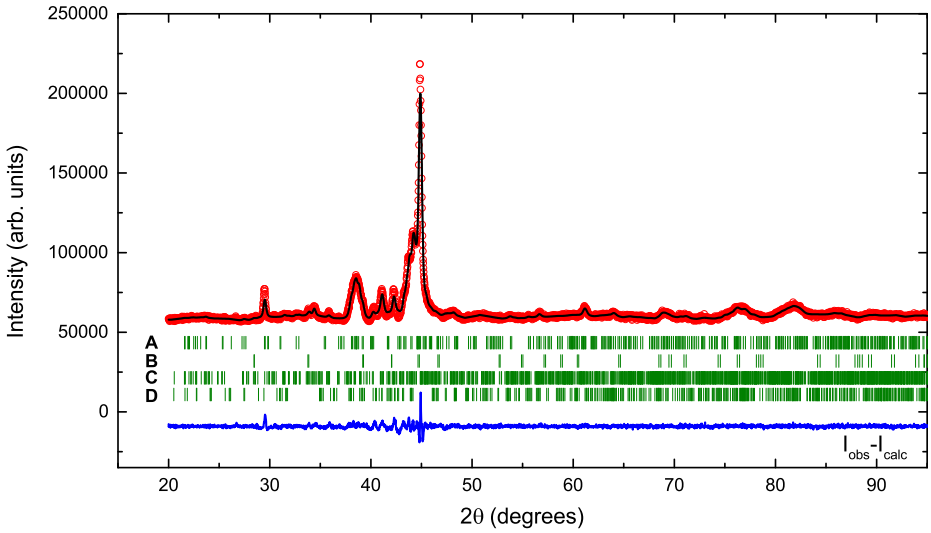


Figure 1: The background subtracted XRD powder pattern in the stoichiometric sample of $ZrNi_3$. The line represents the fit to the measured data. The vertical bars A, B, C and D denote the Bragg angles corresponding to $Zr_2Ni_7$, $ZrNi_3$, $Zr_8Ni_{21}$ and $Zr_7Ni_{10}$, respectively. The bottom line shows the difference between the observed and the fitted pattern.

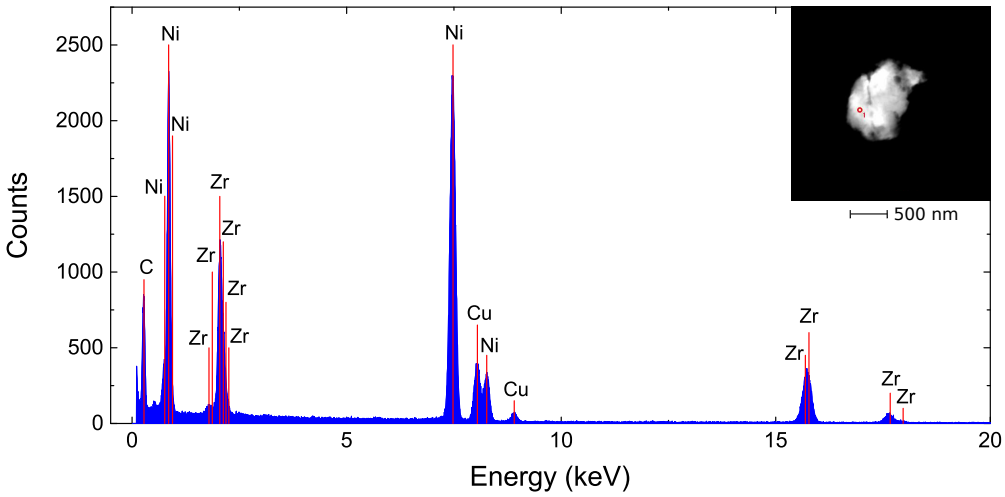


Figure 2: EDX spectrum and TEM image of $ZrNi_3$

in Dhruba reactor, Mumbai by thermal neutron capture with a flux $\sim 10^{13}/\mathrm{cm}^2/\mathrm{s}$ for 7 days. Samples were then sealed in evacuated quartz tubes to carry out measurements at high temperatures. Separate inactive stoichiometric samples of $ZrNi_3$ and $HfNi_3$ were also prepared in similar manners for X-ray diffraction and TEM/energy dispersive X-ray spectroscopy (EDX) measurements. XRD measurements were carried out using the Rigaku X-ray diffractometer TTRAX-III and Cu $K_\alpha$ radiation. Transmission electron microscopy (TEM) measurements were carried out using FEI, Tecnai G2 F30, S-Twin microscope equipped with a high angle annular dark-field (HAADF) de-

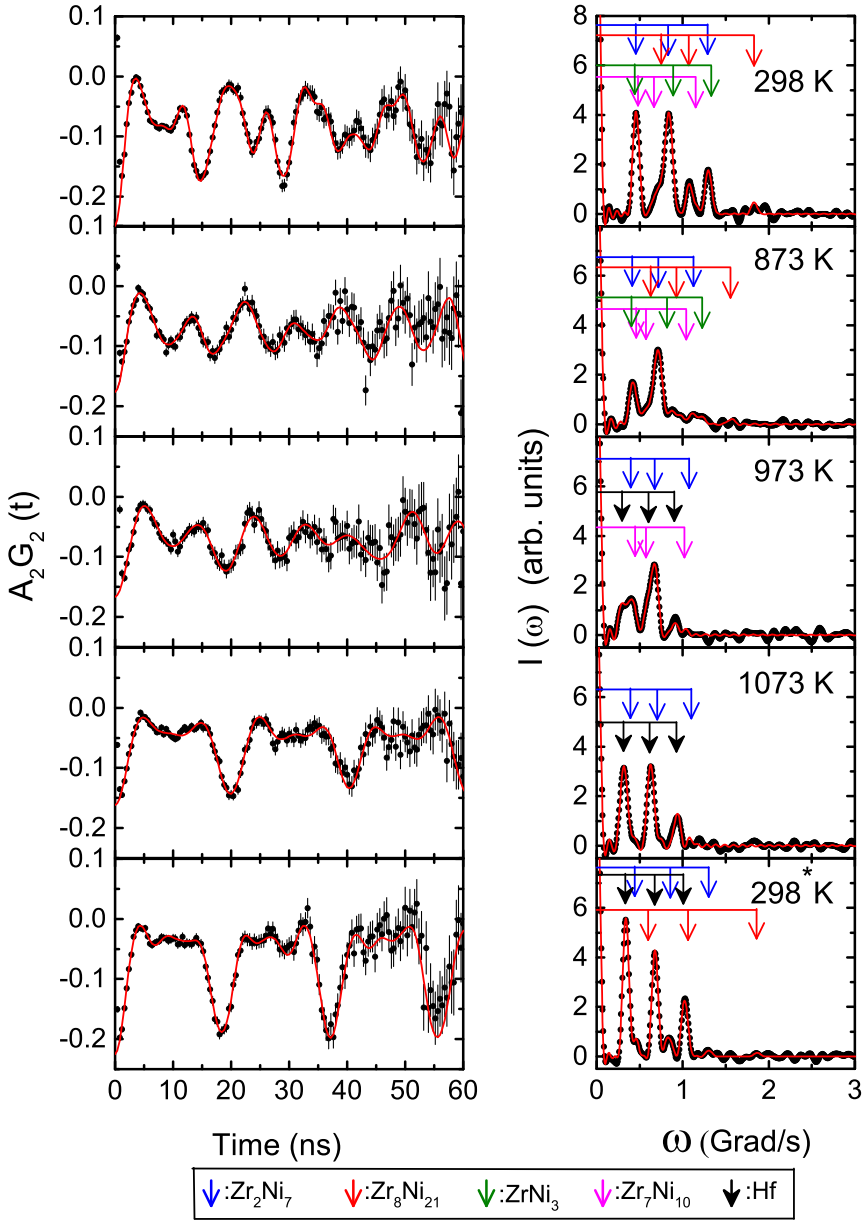


Figure 3: TDPAC spectra in the stoichiometric sample of $ZrNi_3$ at different temperature. Left panel shows the time spectra and the right panel shows the corresponding Fourier cosine transforms. The PAC spectrum at room temperature designated by 298* K is taken after the measurement at 1073 K. A set of three arrows indicates the three transition frequencies of a particular component.

tector, a scanning unit and a energy dispersive X-ray spectroscopy (EDX) unit to perform the scanning transmission electron microscopy (STEM-HAADF-EDX).

The perturbed angular correlation is a nuclear technique to measure the hyperfine interactions between the nuclear moments of the probe nucleus and the hyperfine fields present in the investigated sample. The probe $^{181}$Hf emits two successive $\gamma$-rays, 133 and 482 keV, passing through

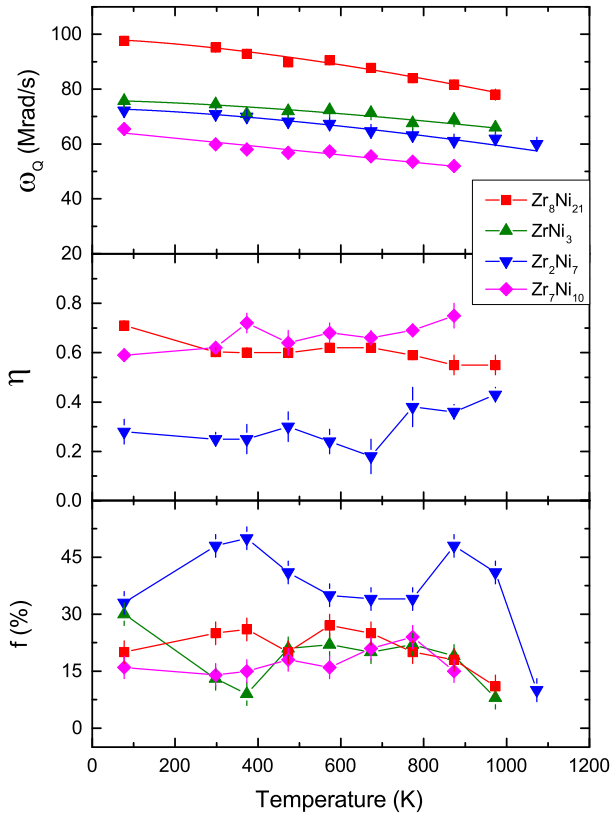


Figure 4: Variations of quadrupole frequency ($\omega_Q$), asymmetry parameter ($\eta$) and site fraction $f(\%)$ with temperature for the components of $Zr_2Ni_7$, $ZrNi_3$, $Zr_8Ni_{21}$ and $Zr_7Ni_{10}$.

the 482 keV intermediate level ($T_{1/2}$=10.8 ns) with a spin angular momentum $I$=5/2$^+\hbar$ [26]. The extra-nuclear electric field gradients present in the sample interact with the nuclear quadrupole moment of the intermediate level ($Q$=2.35 b [26]). Due to this interaction, the angular correlation of the 133-482 keV $\gamma$-$\gamma$ cascade is perturbed. The perturbation function is given by [27],

$$G_2(t) = \Big[S_{20}(\eta) + \sum_{i=1}^{3} S_{2i}(\eta) cos(\omega_i t) exp(-\delta\omega_i t) exp\Big[\frac{-(\omega_i \tau_R)^2}{2}\Big]\Big]. \quad (1)$$

The above expression of perturbation function is valid for a polycrystalline sample and for $I$=5/2$^+$ of intermediate state of the probe nucleus. The frequencies $\omega_i$ are the transition frequencies between different $m$-sublevels arising due to hyperfine splitting. A damping of perturbation function (Lorentzian) was considered through the first exponential which can arise due to structural defects in the sample. Here, $\delta$ is the frequency distribution width. The finite time resolution ($\tau_R$) of the coincidence set up was considered through the second exponential. If more than one quadrupole interaction is present in the sample due to the presence of different component phases or due to two or more non-equivalent sites of a particular phase, the perturbation function can be written as

$$G_2(t) = \sum_i f_i G_2^i(t) \quad (2)$$

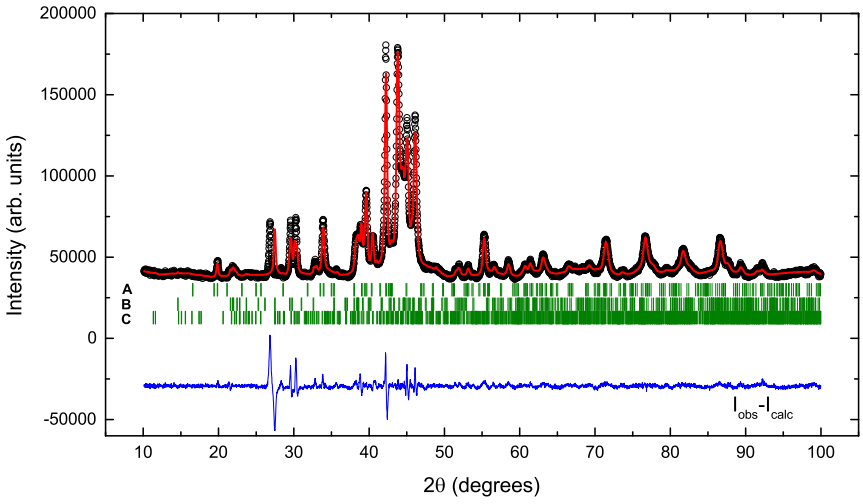


Figure 5: The background subtracted XRD powder pattern in $HfNi_3$. The line represents the fit to the measured data. The vertical bars A, B and C denote the Bragg angles corresponding to $HfNi_3$, $Hf_2Ni_7$ and $Hf_8Ni_{21}$, respectively. The bottom line shows the difference between the observed and the fitted pattern.

where, $f_i$ is the fraction of the $i$-th component and $G_2^i(t)$ is the corresponding perturbation function. A fitting to expression (1) determines the quadrupole frequency $\omega_Q$ through the measured values of $\omega_1$, $\omega_2$ and $\omega_3$. The quadrupole frequency is directly related to the electric field gradient ($V_{zz}$) through the relation

$$\omega_Q = \frac{eQV_{zz}}{4I(2I-1)\hbar}. \tag{3}$$

For an axially symmetric EFG ($\eta$=0), $\omega_Q$ is related to $\omega_1$, $\omega_2$ and $\omega_3$ by $\omega_Q$=$\omega_1/6$=$\omega_2/12$=$\omega_3/18$. The asymmetry parameter is defined as the ratio

$$\eta = \frac{(V_{xx} - V_{yy})}{V_{zz}} \tag{4}$$

and its value lies between 0 and 1. For $\eta \neq$0, this simple relation between $\omega_Q$ and $\omega_i$'s does not hold but, produces a more complex relation [28].

A four detector $LaBr_3$(Ce)-$BaF_2$ set up was used for present TDPAC measurements. The crystal sizes were 38×25 $mm^2$ and 51×51 $mm^2$ for $LaBr_3$(Ce) and $BaF_2$, respectively. The 133 keV $\gamma$-rays were detected in the $LaBr_3$(Ce) detector and the 482 keV $\gamma$-rays were detected in the $BaF_2$ detector. Standard slow-fast coincidence assemblies were employed to acquire four coincidence spectra at $180^o$ and $90^o$ [29]. A typical prompt time resolution (FWHM) of ∼800 ps has been obtained for the energy window settings of $^{181}$Ta $\gamma$-rays. The perturbation function $G_2(t)$ was obtained from the ratio of coincidence counts at $180^o$ and $90^o$. Details on the experimental set up and data acquisition can be found in our earlier report [29].

## 3. PAC Results

### *3.1 Stoichiometric $ZrNi_3$ sample*

The X-ray powder diffraction pattern found in the stoichiometric sample of $ZrNi_3$ is shown in the Figure 1. The present X-ray pattern was best fitted by known crystallographic parameters of $Zr_2Ni_7$

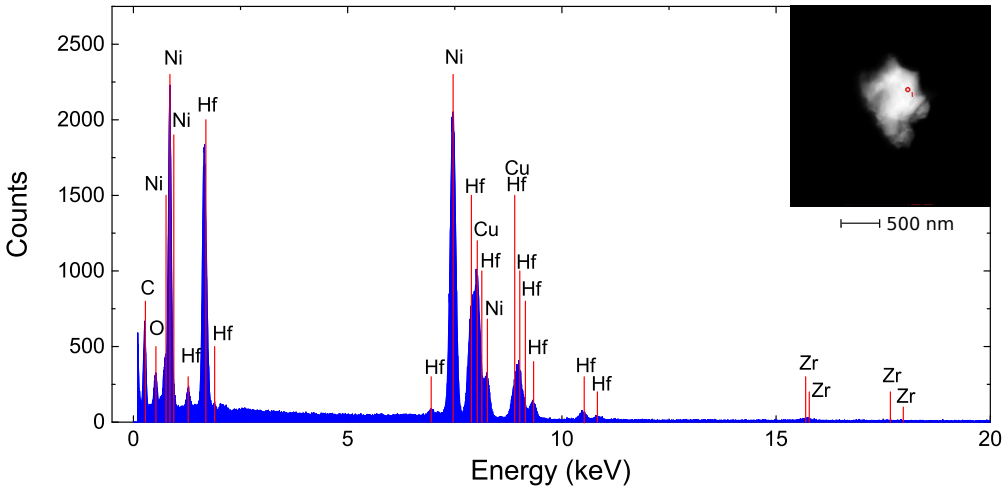


Figure 6: EDX spectrum and TEM image of $HfNi_3$

[31], $ZrNi_3$ [20], $Zr_8Ni_{21}$ [32] and $Zr_7Ni_{10}$ [33]. The contributions of $ZrNi_3$ and $Zr_7Ni_{10}$ were found to be very small compared to $Zr_2Ni_7$ and $Zr_8Ni_{21}$. It can be pointed out that the two stoichiometric samples of $ZrNi_3$ for XRD and PAC measurements are not same. The presence of $ZrNi_3$ phase in this stoichiometric sample of $ZrNi_3$ has been confirmed from TEM/EDX measurement (Figure 2) also. The atomic percentages for Zr and Ni at the indicated spot have been found to be 24.4(3) and 75.6(2), respectively.

The PAC spectrum in the stoichiometric sample of $ZrNi_3$ at room temperature is shown in Figure 3. The spectrum was best fitted by considering four electric quadrupole interactions. The sample produced was found to have non-random orientation of microcrystals and the spectrum was fitted by considering free $S_{2n}$ coefficients. The results of different components found are shown in Table 1. The main frequency component (∼48%) produces values of $\omega_Q$=70.9(2) Mrad/s, $\eta$=0.25(2). This component can be assigned to $Zr_2Ni_7$ by comparing the values of $\omega_Q$ and $\eta$ with the earlier reported results in $Zr_2Ni_7$ [12, 17]. From previous PAC measurements in $ZrNi_5$ also, a similar component to this was obtained and attributed to $Zr_2Ni_7$ [11, 34]. The $ZrNi_5$ has a cubic crystal structure and no EFG at the probe site is expected due to $ZrNi_5$. The component 2 with a symmetric EFG ($\eta$ ∼0) can be attributed to $ZrNi_3$ by comparing with our calculated results from density functional theory (discussed later). The crystal structure of $ZrNi_3$ is hexagonal close-packed and, therefore, a value of $\eta$=0 is expected for this compound. However, this is found to be a minor phase compared to other phases produced in this sample. The results of component 3 can be compared with our recent results in $Zr_8Ni_{21}$ [18]. This component is found to be similar to one component of $Zr_8Ni_{21}$ found from our previous measurements [18] and can, therefore, be attributed to $Zr_8Ni_{21}$. The component 4 can be attributed to $Zr_7Ni_{10}$ by comparing with the results found in $Zr_7Ni_{10}$ [19]. A similar component to this was found in $Zr_8Ni_{21}$ also where it was attributed to $Zr_7Ni_{10}$ [18].

The results of temperature dependent PAC measurements in the stoichiometric $ZrNi_3$ are given in the Table 1. The corresponding TDPAC spectra are shown in Figure 3. It is found that the component fraction due to $ZrNi_3$ is present in the temperature range (77-973 K). At 77 K, the site fraction of $ZrNi_3$ was found to be maximum (∼30%). In the temperature range 77-873 K,

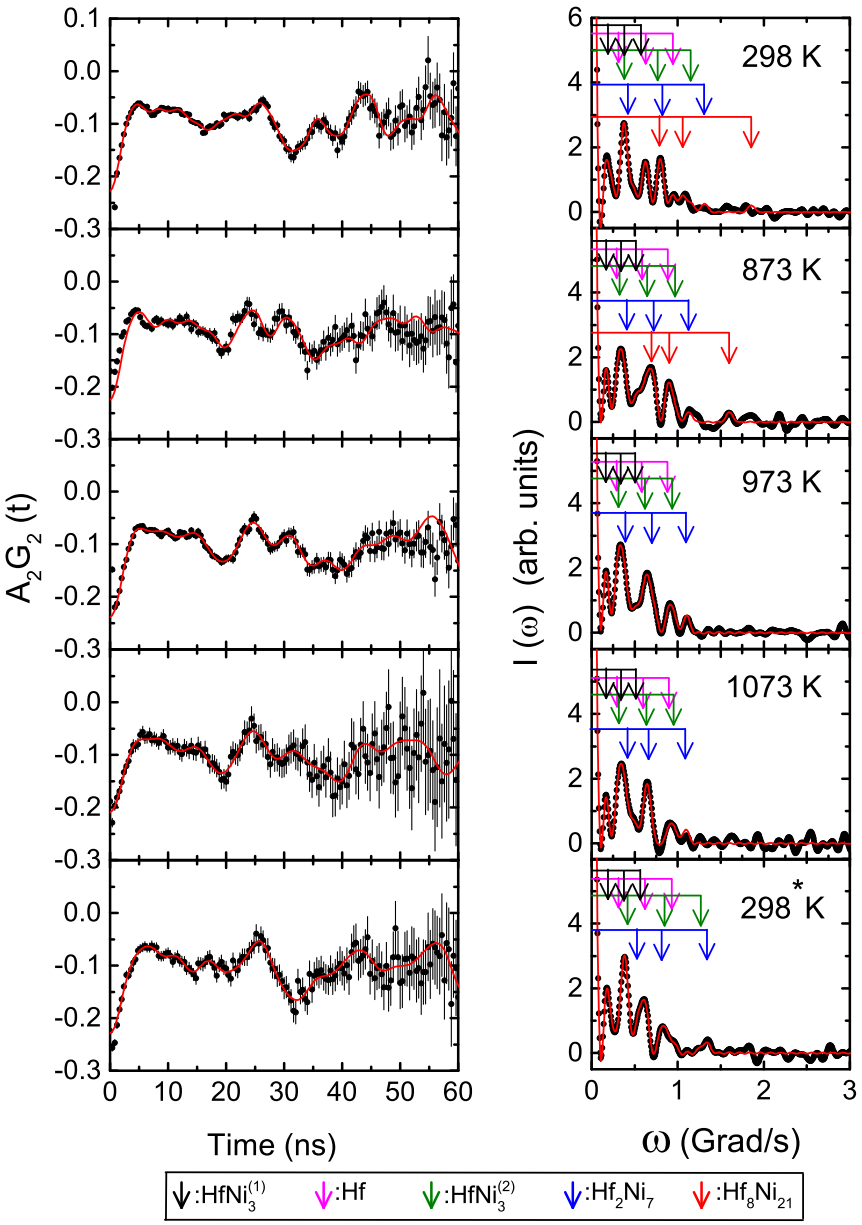


Figure 7: TDPAC spectra in the stoichiometric sample of $HfNi_3$ at different temperature. Left panel shows the time spectra and the right panel shows the corresponding Fourier cosine transforms. The PAC spectrum at room temperature designated by 298* K is taken after the measurement at 1073 K. A set of three arrows indicates the three transition frequencies of a particular component.

four component fractions are found to be present with no appreciable change in parameters. The fractional variations of different components are shown in Figure 4. At 973 K, a distinct change in PAC spectrum has been observed. At this temperature, the component due to $Zr_7Ni_{10}$ disappears. On the other hand, a new frequency component with values of $\omega_Q$=53.0(4) Mrad/s, $\eta$=0 appears. This component is similar to that found in $Zr_8Ni_{21}$ at 1073 K [18]. The site percentage of this

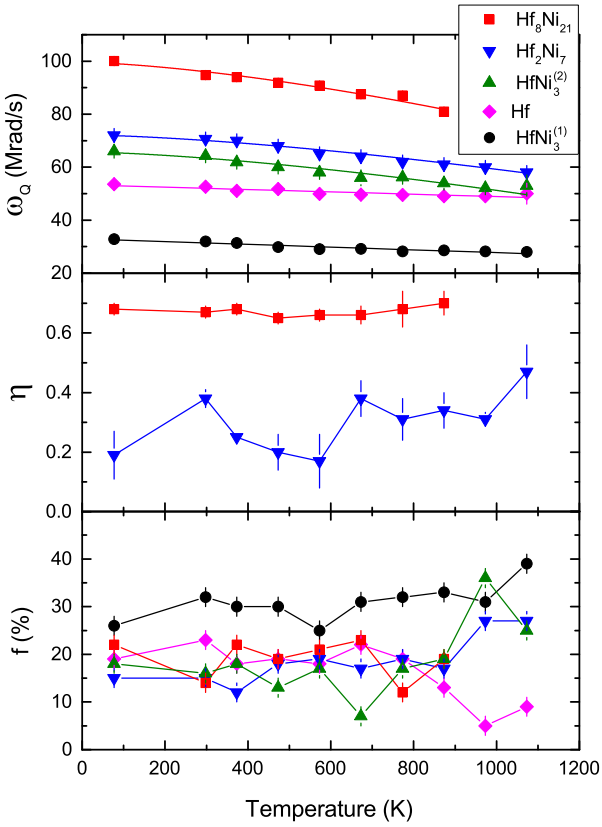


Figure 8: Variations of quadrupole frequency ($\omega_Q$), asymmetry parameter ($\eta$) and site fraction $f(\%)$ with temperature for $HfNi_3^{(1)}$, $HfNi_3^{(2)}$ $Hf_2Ni_7$, $Hf_8Ni_{21}$ and Hf.

new component is found to be ∼39% at this temperature and it enhances abruptly at 1073 K (∼90%). At 1073 K, only two components are found to be present. The minor component found at this temperature is due to $Zr_2Ni_7$. We have repeated the measurement at room temperature after the measurement at 1073 K. The remeasured spectrum at room temperature produces a strong electric quadrupole interaction (∼81%) with values of $\omega_Q$=56.5(1) Mrad/s, $\eta$=0. This component can be recognized as the same component that appeared at 973 and 1073 K. Besides this, two other components are found here. The component due to $Zr_8Ni_{21}$ reappears with a small fraction (∼8%) and the component due to $Zr_2Ni_7$ is also found to be present.

In the present Zr-Ni sample, the predominant component found at 1073 K and subsequently at room temperature can probably be assigned to Hf. At temperatures below 973 K, the probe atoms which were settled at various lattice sites come out from the lattice positions after gaining sufficient energy at high temperature. It seems that at 1073 K, only a small fraction of the probe nucleus (∼10%) is attached with the Zr-Ni compounds. A similar phenomenon was observed from our recent PAC investigation in $Zr_8Ni_{21}$ [18].

The evolution of quadrupole frequency, asymmetry parameter and site fraction with temperature for different components observed are shown in Figure 4. It is found that quadrupole frequencies for the components $Zr_2Ni_7$, $ZrNi_3$ and $Zr_8Ni_{21}$ vary with temperature following $T^{3/2}$ relationship. For the $Zr_8Ni_{21}$ component, a similar temperature dependent behavior was observed

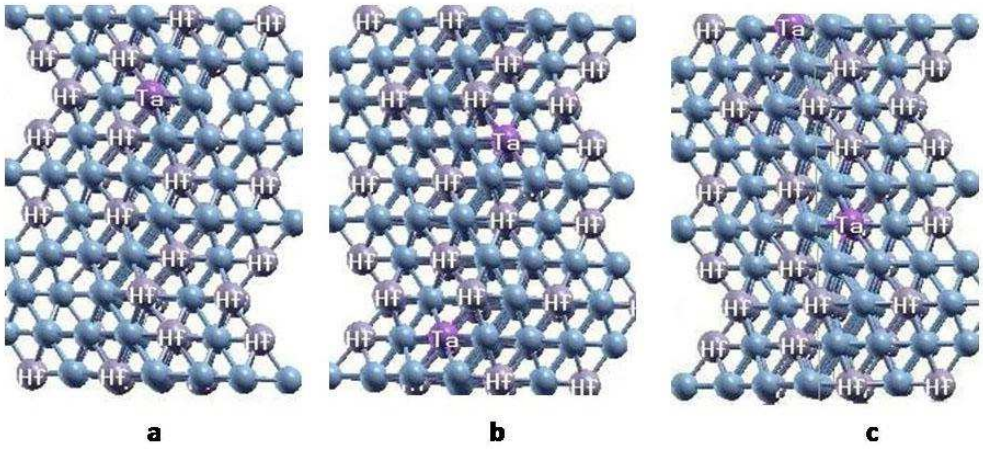


Figure 9: Models of cells used in the study of $HfNi_3$

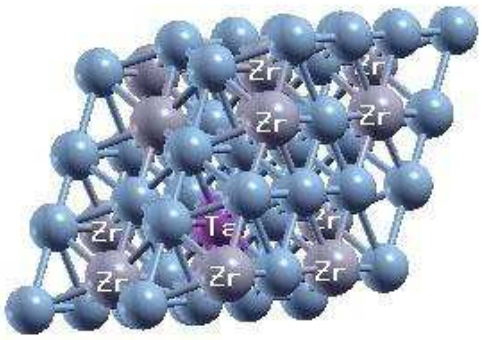


Figure 10: Model of cell used in the study of $ZrNi_3$

from our previous PAC investigation in $Zr_8Ni_{21}$ [18]. For these three components, values of $\omega_Q$ have been fitted using the relation

$$\omega_Q(T) = \omega_Q(0)[1 - \beta T^{3/2}] \tag{5}$$

where, $\omega_Q(0)$ is the extrapolated value at 0 K. The results of $\eta$ and site fraction for different components are also plotted (Figure 4). These results do not show large variations except the site fraction of $Zr_2Ni_7$ which decreases drastically at 1073 K ($\sim$10%) compared to the fraction found at 973 K ($\sim$41%). The fitted results are listed in Table 2. Contrary to these, $\omega_Q$ for the component $Zr_7Ni_{10}$ is found to obey a linear temperature dependent behavior. In this case, we have fitted the results of $\omega_Q(T)$ using the relation

$$\omega_Q(T) = \omega_Q(0)[1 - \alpha T]. \tag{6}$$

Both $T^{3/2}$ and $T$ variations of EFG (proportional to $\omega_Q$) for metallic and intermetallic systems are found in literature [35].

*3.2 Stoichiometric $HfNi_3$ sample*

The XRD measurement in the stoichiometric sample of $HfNi_3$ has been carried out at room temperature (Figure 5). Analysis of the X-ray powder pattern was done using the known crystallographic data of $HfNi_3$ for low temperature phase [25], $Hf_2Ni_7$ [36] and $Hf_8Ni_{21}$ [37]. The X-ray spectrum shows that major contribution comes from $HfNi_3$. It was reported [30] that high temperature phase of $HfNi_3$ was formed from the melt and $Hf_2Ni_7$ by peritectic reaction. Apart from $HfNi_3$, there are phases due to $Hf_2Ni_7$ and $Hf_8Ni_{21}$. But, no prominent peak due to $Hf_7Ni_{10}$ was found in the XRD spectrum. The phase $HfNi_3$ has been confirmed from our TEM/EDX measurement also (Figure 6). The atomic percentages for Hf and Ni at the indicated spot have been found to be 24.4(2) and 74.3(2), respectively.

The PAC spectrum observed in $HfNi_3$ at room temperature after preparing the sample in argon arc furnace is shown in Figure 7. It is found that five electric quadrupole frequencies are required to fit the time spectrum. Analysis was done by considering free $S_{2n}$ coefficients. The major component (∼32%) found with values of $\omega_Q$=32.0(3) Mrad/s, $\eta$=0 (Table 3) can be attributed to $HfNi_3$ by comparing with our calculated results from DFT (discussed later). From our previous studies in $Hf_8Ni_{21}$ [18] and $Hf_7Ni_{10}$ [19], a component similar to this was observed and tentatively assigned to $HfNi_3$. Component 2 can also be attributed to $HfNi_3$ because the values of EFG and asymmetry parameter for this component are found to be in good agreement with the calculated results from DFT (discussed later). The component 3 has been attributed to $Hf_2Ni_7$ by comparing with the earlier reported results in $Hf_2Ni_7$ [11, 12]. From previous PAC measurement in $HfNi_5$, a similar component to this was also found and attributed to $Hf_2Ni_7$ [11]. The component 4 (∼14%) with values of $\omega_Q$=94.8(6) Mrad/s and $\eta$=0.67(2) can be assigned to $Hf_8Ni_{21}$. From our recent investigation in $Hf_8Ni_{21}$ [18], similar values of quadrupole frequency and asymmetry parameter were found. In $Hf_8Ni_{21}$, however, two non-equivalent Hf sites were found. But, in this stoichiometric $HfNi_3$ sample, we have found only one site of $Hf_8Ni_{21}$. The other non-equivalent site of $Hf_8Ni_{21}$ is not observed here. Besides these, a component with symmetric EFG (component 5) was found which can be attributed to pure hcp Hf by comparing the values of $\omega_Q$ and $\eta$ with earlier reported results [38]. Probably, this component arises due to unreacted Hf with Ni. Decrease of this component at 973 and 1073 K indicates that more Hf reacts with Ni to form compounds at high temperatures.

Temperature dependent PAC results are given in Table 3. The corresponding PAC spectra are shown in Figure 7. In the temperature range 77-873 K, there are no appreciable changes in the PAC spectra. At 973 K, the component $Hf_8Ni_{21}$ disappears. The component due to $Hf_8Ni_{21}$ does not appear at 1073 K also. But other four components are found to exist at 1073 K. However, unlike stoichiometric $ZrNi_3$, no additional component is observed at 1073 K. The PAC measurement was then repeated at room temperature. At this temperature, two components of $HfNi_3$ reappear which indicates that $HfNi_3$ is a stable phase. The component $Hf_8Ni_{21}$ does not appear when remeasured at room temperature. The components of $Hf_2Ni_7$ and Hf are found to be present when remeasured at room temperature.

The evolution of the quadrupole frequency, $\eta$ and site fraction with temperature for the different components observed in stoichiometric $HfNi_3$ are shown in Figure 8. The components $Hf_8Ni_{21}$ and $Hf_2Ni_7$ follow the same $T^{3/2}$ temperature dependence as found for $Zr_8Ni_{21}$ and $Zr_2Ni_7$ in $ZrNi_3$. The EFG for the two components of $HfNi_3$ are found to vary different manner. The quadrupole frequency of $HfNi_3^{(2)}$ varies with temperature following $T^{3/2}$ relationship (Eqn. 5). On the other hand, a linear temperature dependent behavior (Eqn. 6) was found for the $HfNi_3^{(1)}$ component.

Variation of the quadrupole frequency for the hexagonal Hf was also found to be linear. The fitted results are shown in Table 2. The variations of $\eta$ and site fractions for different components do not show large changes (Figure 8).

## 4. DFT calculations

The first-principles density functional theory (DFT) calculations were performed with the WIEN2k simulation package [39] based on the full potential (linearized) augmented plane waves method (FP (L)APW). Electronic exchange-correlation energy was treated with generalized gradient approximation (GGA) parametrized by Perdew-Burke-Ernzerhof (PBE) [40]. In our calculations the muffin-tin radii for Hf, Ni, Zr and Ta were 2.3, 2.1, 2.3 and 2.3 a. u., respectively. The cut-off parameter $R_{mt}K_{max}$ for limiting the number of plane waves was set to 7.0, where $R_{mt}$ is the smallest value of all atomic sphere radii and $K_{max}$ is the largest reciprocal lattice vector used in the plane wave expansion.

The Brillouin zone integrations within the self-consistency cycles were performed via a tetrahedron method [41], using 6-50 $k$ points in the irreducible wedge of the Brillouin zone (4×4×2 and 8×8×8 meshes for Ta doped $HfNi_3$ and $ZrNi_3$, respectively) for the supercell calculations. The atomic positions were relaxed according to Hellmann-Feynman forces calculated at the end of each self-consistent cycle, with the force minimization criterion 2 mRy/a.u.. In our calculations the self-consistency was achieved by demanding the convergence of the integrated charge difference between last two iterations to be smaller than $10^{-5}$ $e$. All the calculations refer to zero temperature.

### *4.1 HfNi$_3$*

$HfNi_3$ at the temperatures below 1200°C, has the $\gamma$-Ta(Pd,Rh)$_3$-type structure, with a stacking of ten $AB_3$ layers in the sequence ABCBCACBCB. The space group is $P6_3/mmc$ and the unit cell dimensions are $a$=5.2822(2), $c$=21.3916(18) $\mathring{A}$ at room temperature [25]. This structure contains 40 atoms in the unit cell, distributed at 6 non-equivalent crystallographic positions, 3 for Hf atoms and 3 for Ni atoms (Table 5).

After obtaining the optimized structural parameters, we constructed 2×2×1 supercell from periodically repeating unit cells of the host crystals. To simulate PAC measurements at Hf1 position, we replaced one Hf atom in the supercell at the position (0 0 1/4) with Ta (Figure 9a [42]). In the case of Ta at the Hf2 and Hf3 positions due to the complexity of the calculations, we had to replace two Hf atoms at the corresponding position with Ta, thus obtaining the cell with 50 non-equivalent atoms (Figure 9b and c). We checked that the two Ta atoms are sufficiently far from each other (11.1 $\mathring{A}$) to avoid significant impurity-impurity interactions. After determing the self-consistent charge density we obtain the electric field gradient (EFG) tensor $V_{ij}$ using the method developed in reference [43]. The usual convention is to designate the largest component of the EFG tensor as $V_{zz}$. The asymmetry parameter $\eta$ is then given by $\eta$= ($V_{xx}$-$V_{yy}$)/$V_{zz}$, where $|V_{zz}| \geq |V_{yy}| \geq |V_{xx}|$. All the calculations refer to zero temperature.

The theoretically determined cell and structure parameters for the investigated structure, along with the experimental values obtained from X-ray diffraction measurements are given in Table 4. The theoretical volume slightly overestimates the experimental one. The bulk modulus $B_0$, obtained by fitting the data to the Murnaghan's equation of state [44] is also given in Table 4. The calculated interatomic distances, given in Table 5, are also slightly larger than the measured ones, but the overall agreement is good.

The calculated EFGs in the pure compound as well as at Ta probe position in the $\beta$-$HfNi_3$ are given in Table 6. It can be observed that EFG is smallest at Hf1 position and the largest at Hf2 position. This trend preserves also for the electric field gradients calculated at corresponding Ta positions, but the EFGs are now larger from 30% to 60%. We see that the calculated result for EFG at the Ta probe site replacing Hf3 atom ($3.5\times10^{21}$ V/m$^2$) is in excellent agreement with the measured value of EFG=$3.68\times10^{21}$ V/m$^2$ ($\omega_Q(0)$=32.9 Mrad/s) for the component $HfNi_3^{(1)}$, thus confirming that the mentioned component of the measuered PAC spectra originates from $HfNi_3$. Similarly, the calculated results at the Ta probe site replacing Hf2 atom ($V_{zz}$=$7.1\times10^{21}$ V/m$^2$ and $\eta$=0) are in excellent aggrement with our measured values of $HfNi_3^{(2)}$ component ($V_{zz}(0)$=$7.3\times10^{21}$ V/m$^2$ and $\eta$=0) which confirms that this component also originates from $HfNi_3$.

*4.2 $ZrNi_3$*

$ZrNi_3$ crystallizes in the hexagonal $Ni_3Sn$ type structure, which possesses two non-equivalent crystallographic positions, Zr 2c and Ni 6h [20]. The optimized lattice constants, which slightly overestimate the experimental values, are given in Table 4. The calculated EFG at Zr position is -$3.0\times10^{21}$ V/m$^2$, with zero asymmetry parameter. In order to simulate PAC measurement, we constructed 2×2×2 supercell from periodically repeating unit cell and then replaced one of the Zr atoms by Ta (Figure 10 [42]). The point group symmetry around the impurity Ta atom remained the same as around the original Zr atom, but the number of non-equivalent positions increased. The calculated EFG at the Ta probe atom -$8.4\times10^{21}$ V/m$^2$ is in excellent agreement with two mutually similar EFG values from measured PAC spectra (8.2 and $8.48\times10^{21}$ V/m$^2$, corresponding to $\omega_Q(0)$= 72.9 and 76 Mrad/s, respectively). The fact that the corresponding calculated asymmetry parameter is zero, enables us to assign the 76 Mrad/s component to $ZrNi_3$ and thus definitely confirm the presence of this phase in our stoichiometric sample.

## 5. Conclusion

From TDPAC and XRD measurements, multiple phases have been found in the stoichiometric samples of $ZrNi_3$ and $HfNi_3$. The presence of $ZrNi_3$ and $HfNi_3$ in these stoichiometric samples have been confirmed from TDPAC, XRD and TEM/EDX measurements. From PAC studies, it is found that $ZrNi_3$ is produced as a minor phase while the phase $HfNi_3$ is found to be largely produced. Also, our temperature dependent PAC studies show that $HfNi_3$ is a very stable phase. In the stoichiometric samples of $ZrNi_3$ and $HfNi_3$, secondary phases due to $(Zr/Hf)_8Ni_{21}$ and $(Zr/Hf)_2Ni_7$ are found to be produced. In $ZrNi_3$, the phase due to $Zr_7Ni_{10}$ is observed while no phase due to $Hf_7Ni_{10}$ is found in $HfNi_3$ sample. Only one and the same crystallographic site of $(Zr/Hf)_8Ni_{21}$ is found in present stoichiometric samples of $ZrNi_3$ and $HfNi_3$ although two non-equivalent sites were found in $(Zr/Hf)_8Ni_{21}$ [18]. The experimental values of EFG and $\eta$ for $ZrNi_3$ and $HfNi_3$ are found to be in excellent agreement with the theoretically calculated values of EFG and $\eta$ at $^{181}$Ta impurity sites by the first-principles density functional theory based on the FP (L)APW. From our calculation, three non-equivalent Hf sites in $HfNi_3$ have been found whereas two of these have been observed from PAC measurements. In $ZrNi_3$, on the other hand, the present DFT calculation produces one EFG corresponding to a single Zr site. From our PAC measurements in $ZrNi_3$ also, a single frequency component has been found.

The solubility of Hf in Ni is found to be less compared to Zr in Ni. The Hf solubility in Ni is found to increase with temperature and it decreases again when the temperature is lowered. In

Zr-Ni compounds, the binding energy of Hf probe to the lattice sites is not strong enough at high temperature and, probably, the probe atoms are detached from the compound at ∼1000 K.

The TDPAC is found to be an useful nuclear technique to detect weak component phases that are produced in a material. Particularly, a $LaBr_3$(Ce)-$BaF_2$ set up is found to be very useful for separating the minor component phases when multiple components are present in the sample.


## Acknowledgement

The help of Prof. Dr. T. Butz, University of Leipzig, Germany in data analysis is gratefully acknowledged with thanks. We are grateful to Dr. B. Satpati of SINP, Kolkata for TEM/EDX measurements and analysis. We would like to thank A. Karmahapatra and S. Pakhira of SINP, Kolkata for their helps in XRD measurements and data analysis. The present work is supported by the Department of Atomic Energy, Government of India through the Grant no. 12-R&D-SIN-5.02-0102. J. Belošević-Čavor and D. Toprek acknowledge support by The Ministry of Education, Science and Technological Department of the Republic of Serbia through the Grant no. 171001.


## References


[1] J. Nei, K. Young, S. O. Salley, K. Y. S. Ng, J. Alloys Compd. 516 (2012) 144.
[2] J.M. Joubert, M. Latroche, A. Percheron-Guègan, J. Alloys Compd. 231 (1995) 494.
[3] F.C. Ruiz, E.B. Castro, S.G. Real, H.A. Peretti, A. Visintin, W.E. Triaca, Int. J. Hydrogen Energy, 33 (2008) 3576.
[4] F. C. Ruiz, E. B. Castro, H. A. Peretti, A. Visitin, Int. J. Hydrogen Energy 35 (2010) 9879.
[5] J. Nei, K. Young, R. Regmi, G. Lawes, S.O. Salley, K.Y.S. Ng, Int. J. Hydrogen Energy 37 (2012) 16042.
[6] Kwo-hsiung Young, Jean Nei, Materials 6 (2013) 4574.
[7] R. B. Wright, J. G. Jolley, M. Owens, D. L. Cocke, J. Vac. Sci. Tech. A5 (1987) 586.
[8] J. A. Davidson, Titanum molybdenum hafnium alloys for medical implants and devices, US Patent 5954724 (Sept. 21, 1999).
[9] X. L. Meng, Y. D. Fu, W. Cai, Q. F. Li and L. C. Zhao, Phil. Mag. Lett. 89 (2009) 431.
[10] A. Baudry, P. Boyer, L.P. Pontonnier, J. Phys. Conden. Matt. 4 (1992) 5025.
[11] P.R.J. Silva, H. Saitovitch, J.T. Cavalcante, M. Forker, J. Magn. Magn. Mater. 322 (2010) 1841.
[12] M. Marszalek, H. Saitovitch, P.R.J. Silva, Z. Naturforsch. 55a (2000) 49.
[13] B. Wodnecka, M. Marszalek, P. Wodniecki, A.H. Hrynkiewicz, Hyperfine Interact. 80 (1993) 1039.
[14] A.N. Poynor, S.E. Cumblidge, R.L. Rasera, G.L. Catchen, A.T. Mota, Hyperfine Interact. 136/137 (2001) 549.
[15] A. Umícevíc, B. Cekíc, V. Ivanovski, V Koteski, J. Belošević-Čavor[2], M. Šiljegovíc, S. Pavlovíc, J. Alloys Compd. 475 (2009) 38.
[16] B. Cekíc, A. Umícevíc, V. Ivanovski, V. Koteski, J. Belošević-Čavor[2], S. Pavlovíc, J. Alloys Compd. 480 (2009) 40.
[17] C.C. Dey and S. K. Srivastava, Physica B 427 (2013) 126.
[18] S. K. Dey, C. C. Dey, S. Saha, J. Belošević-Čavor, Intermetallics 84 (2017) 112.
[19] S. K. Dey, C. C. Dey, S. Saha, J. Belošević-Čavor (to be published).
[20] C. Becle, B. Bourniquel, G. Develey and M. Saillard, J. Less Comm. Metals 66 (1979) 59.
[21] E. Smith and R. W. Guard, Trans. Metall. Soc. AIME 209 (1957) 1189.
[22] D. Kramer, Trans. Metall. Soc. AIME 251 (1959) 256.
[23] M. E. Kirkpatrick and W. L. Larson, Trans. Am. Soc. Met. 54 (1961) 580.
[24] J. H. N. Van Vucht, J. Less-Common Met., 11 (1966) 308.
[25] L. Bsenko, Acta Crystallogr. B 34 (1978) 3201.
[26] N. J. Stone, At. Data Nucl. Data Tables 90 (2005) 75.
[27] G. Schatz and A. Weidinger, in: Nuclear condensed matter physics; nuclear methods and application translated by J. A. Gardner (John Wiley and Sons, Chichester, New York, Brisbane, Toronto, Singapore 1996) chapter 5, p. 63.

[28] Matthew Zacate and Herbert Jaeger, Defect and Diffusion Forum 311 (2011) 3
[29] C. C. Dey, Pramana 70, 835 (2008).
[30] Lars Bsenko, J. Less Common Met. 63 (1979) 171.
[31] F.R. Eshelman and J.F. Smith, Acta Cryst. B28 (1972) 1594.
[32] J. M. Joubert, R. cernỳ, K. Yvon, Z. Kristallogr. New Cryst. Struct. 213 (1998) 227.
[33] J.-M. Joubert, R. Černý, K. Yvon, M. Latroche, A.P. Guégan, Acta Crystallogr. C 53 (1997) 1536.
[34] C.C. Dey, J. Magn. Magn. Mater. 342 (2013) 87.
[35] W. Witthuhn and E. Engel, in Hyperfine Interactions of Radioactive Nuclei, Ed. by J. Christiansen (Springer-Verlag Berlin Heidelberg New York Tokyo, 1983) P. 205.
[36] J.P. Dattagupta, K. Schubert, Z. Metallkd. 64 (1973) 789.
[37] Lars Bsenko, Acta Cryst. B34 (1978) 3204.
[38] S. K. Dey, C. C. Dey, S. Saha, J. Phys. Chem. Solids 95 (2016) 98.
[39] P. Blaha, K. Schwarz, G. K. H. Madsen, D. Kvasnicka, J. Luitz, WIEN 2k an Augmented Plane Wave Plus Local Orbitals Program for Calculating Crystal Properties, Vienna University of Technology, Vienna, Austria, 2001.
[40] J. P. Perdew, S. Burke, M. Ernzerhof, Generalized Gradient Approximation Made Simple, Physical Review Letters 77 (1996) 3865.
[41] P. E. Blochl, O. Jepsen, O. K. Andersen, Improved tetrahedron method for Brillouin-zone integrations, Physical Review B 49 (1994) 16223.
[42] A. Kokalj, J. Mol. Graphics Modelling 17 (1999) 176.
[43] P. Blaha, K. Schwarz, First-Principles Calculation of the Electric Field Gradient of $Li_3N$, Physical Review Letters. 54 (1985) 1192.
[44] F. D. Murnaghan, Proc. Natl. Acad. Sci. U. S. A. 30 (1944) 244.
[45] J. Anubhav, S. Ping Ong, G. Hautier, W. Chen, W. Davidson Richards, S. Dacek, C. Shreyas, D. Gunter, D. Skinner, G. Ceder, K. Persson, The Materials Project: A materials genome approach to accelerating materials innovation, APL Materials 1 (2013) 011002.

Table 1: Results of PAC measurements in stoichiometric sample of $ZrNi_3$

| Temperature (K) | Component | $\omega_Q$ (Mrad/s) | $\eta$ | $\delta$(%) | $f$(%) | Assignment |
|---|---|---|---|---|---|---|
| 77 | 1 | 72.2(9) | 0.28(5) | 0 | 33(3) | $Zr_2Ni_7$ |
| | 2 | 75.7(8) | 0 | 0 | 30(3) | $ZrNi_3$ |
| | 3 | 97.6(6) | 0.71(2) | 0 | 20(3) | $Zr_8Ni_{21}$ |
| | 4 | 65.5(8) | 0.59(2) | 0 | 16(3) | $Zr_7Ni_{10}$ |
| 298 | 1 | 70.9(2) | 0.25(2) | 0 | 48(3) | $Zr_2Ni_7$ |
| | 2 | 74.5(9) | 0 | 0 | 13(3) | $ZrNi_3$ |
| | 3 | 95.2(3) | 0.603(8) | 0 | 25(3) | $Zr_8Ni_{21}$ |
| | 4 | 59.9(5) | 0.62(2) | 0 | 14(3) | $Zr_7Ni_{10}$ |
| 373 | 1 | 69.9(3) | 0.25(6) | 0 | 50(3) | $Zr_2Ni_7$ |
| | 2 | 71(2) | 0 | 0 | 9(3) | $ZrNi_3$ |
| | 3 | 92.9(6) | 0.60(2) | 0 | 26(3) | $Zr_8Ni_{21}$ |
| | 4 | 58(1) | 0.72(4) | 0 | 15(3) | $Zr_7Ni_{10}$ |
| 473 | 1 | 68.2(4) | 0.30(6) | 0 | 41(3) | $Zr_2Ni_7$ |
| | 2 | 72(1) | 0 | 0 | 21(3) | $ZrNi_3$ |
| | 3 | 89.8(8) | 0.60(2) | 0 | 20(3) | $Zr_8Ni_{21}$ |
| | 4 | 56.8(8) | 0.64(5) | 0 | 18(3) | $Zr_7Ni_{10}$ |
| 573 | 1 | 67.3(4) | 0.24(5) | 0 | 35(3) | $Zr_2Ni_7$ |
| | 2 | 72.4(8) | 0 | 0 | 22(3) | $ZrNi_3$ |
| | 3 | 90.5(5) | 0.62(1) | 0 | 27(3) | $Zr_8Ni_{21}$ |
| | 4 | 57.3(9) | 0.68(4) | 0 | 16(3) | $Zr_7Ni_{10}$ |
| 673 | 1 | 64.6(4) | 0.18(7) | 0 | 34(3) | $Zr_2Ni_7$ |
| | 2 | 71.3(9) | 0 | 0 | 20(3) | $ZrNi_3$ |
| | 3 | 87.7(6) | 0.62(2) | 0 | 25(3) | $Zr_8Ni_{21}$ |
| | 4 | 55.5(8) | 0.66(3) | 0 | 21(3) | $Zr_7Ni_{10}$ |
| 773 | 1 | 63.1(6) | 0.38(8) | 0 | 34(3) | $Zr_2Ni_7$ |
| | 2 | 67.6(5) | 0 | 0 | 22(3) | $ZrNi_3$ |
| | 3 | 84.0(5) | 0.59(1) | 0 | 20(3) | $Zr_8Ni_{21}$ |
| | 4 | 53.5(4) | 0.69(2) | 0 | 24(3) | $Zr_7Ni_{10}$ |
| 873 | 1 | 61.1(2) | 0.36(3) | 0 | 48(3) | $Zr_2Ni_7$ |
| | 2 | 68.8(8) | 0 | 0 | 19(3) | $ZrNi_3$ |
| | 3 | 81.7(9) | 0.55(4) | 0 | 18(3) | $Zr_8Ni_{21}$ |
| | 4 | 52(1) | 0.75(5) | 0 | 15(3) | $Zr_7Ni_{10}$ |
| 973 | 1 | 60.3(5) | 0.43(3) | 0 | 41(2) | $Zr_2Ni_7$ |
| | 2 | 53.0(4) | 0 | 0 | 39(2) | Hf |
| | 3 | 66(2) | 0 | 0 | 8(2) | $ZrNi_3$ |
| | 4 | 78(2) | 0.55(4) | 0 | 11(2) | $Zr_8Ni_{21}$ |
| 1073 | 1 | 52.0(1) | 0 | 0 | 90(2) | Hf |
| | 2 | 60(1) | 0.31(5) | 0 | 10(2) | $Zr_2Ni_7$ |
| 298[†] | 1 | 56.5(1) | 0 | 0 | 81(2) | Hf |
| | 2 | 71.9(8) | 0.19(5) | 0 | 11(2) | $Zr_2Ni_7$ |
| | 3 | 95(1) | 0.65(3) | 0 | 8(2) | $Zr_8Ni_{21}$ |

[†] after measurement at 1073 K

Table 2: Results of temperature dependent variations of $\omega_Q$ for different components in the stoichiometric samples of $ZrNi_3$ and $HfNi_3$.

| Component phases | $\omega_Q(0)$ (Mrad/s) | $V_{zz}(0)$ ($\times 10^{21}$) V/m$^2$ | $\alpha$ ($\times 10^{-4}$) K$^{-1}$ | $\beta$ ($\times 10^{-6}$) K$^{-3/2}$ |
|---|---|---|---|---|
| $Zr_2Ni_7$ | 72.9(4) | 8.2(1) | | 6.2(4) |
| $ZrNi_3$ | 76(1) | 8.48(9) | | 4.3(6) |
| $Zr_8Ni_{21}$ | 98.2(5) | 11.0(2) | | 6.5(3) |
| $Zr_7Ni_{10}$ | 64(2) | 7.28(5) | 2.3(3) | |
| $HfNi_3^{(1)}$ | 32.9(4) | 3.68(3) | 1.6(2) | |
| $HfNi_3^{(2)}$ | 65.7(4) | 7.3(1) | | 7.0(4) |
| $Hf_2Ni_7$ | 72.2(4) | 8.1(1) | | 5.7(2) |
| $Hf_8Ni_{21}$ | 99.3(6) | 11.1(2) | | 6.6(4) |
| Hf | 53.3(6) | 5.95(6) | 0.8(2) | |

Table 3: Results of PAC measurements in the stoichiometric $HfNi_3$ sample

| Temperature (K) | Component | $\omega_Q$ (Mrad/s) | $\eta$ | $\delta$(%) | $f$(%) | Assignment |
|---|---|---|---|---|---|---|
| 77 | 1 | 32.8(7) | 0 | 0 | 26(2) | $HfNi_3^{(1)}$ |
| | 2 | 66.0(7) | 0 | 0 | 18(2) | $HfNi_3^{(2)}$ |
| | 3 | 72(1) | 0.19(8) | 0 | 15(2) | $Hf_2Ni_7$ |
| | 4 | 100.1(5) | 0.68(2) | 0 | 22(2) | $Hf_8Ni_{21}$ |
| | 5 | 53.6(8) | 0 | 0 | 19(2) | Hf |
| 298 | 1 | 32.0(3) | 0 | 0 | 32(2) | $HfNi_3^{(1)}$ |
| | 2 | 64.3(8) | 0 | 0 | 16(2) | $HfNi_3^{(2)}$ |
| | 3 | 70.6(6) | 0.38(3) | 0 | 15(2) | $Hf_2Ni_7$ |
| | 4 | 94.8(6) | 0.67(2) | 0 | 14(2) | $Hf_8Ni_{21}$ |
| | 5 | 52.6(4) | 0 | 0 | 23(2) | Hf |
| 373 | 1 | 31.4(5) | 0 | 0 | 30(2) | $HfNi_3^{(1)}$ |
| | 2 | 61.9(7) | 0 | 0 | 18(2) | $HfNi_3^{(2)}$ |
| | 3 | 70(1) | 0.25(fixed) | 0 | 12(2) | $Hf_2Ni_7$ |
| | 4 | 94.0(6) | 0.68(2) | 0 | 22(2) | $Hf_8Ni_{21}$ |
| | 5 | 51.1(7) | 0 | 0 | 18(2) | Hf |
| 473 | 1 | 29.8(4) | 0 | 0 | 30(2) | $HfNi_3^{(1)}$ |
| | 2 | 60(1) | 0 | 0 | 13(2) | $HfNi_3^{(2)}$ |
| | 3 | 67.9(6) | 0.20(6) | 0 | 18(2) | $Hf_2Ni_7$ |
| | 4 | 91.9(6) | 0.65(2) | 0 | 19(2) | $Hf_8Ni_{21}$ |
| | 5 | 51.7(7) | 0 | 0 | 19(2) | Hf |
| 573 | 1 | 29.1(6) | 0 | 0 | 25(2) | $HfNi_3^{(1)}$ |
| | 2 | 58(1) | 0 | 0 | 17(2) | $HfNi_3^{(2)}$ |
| | 3 | 65(1) | 0.17(9) | 0 | 19(2) | $Hf_2Ni_7$ |
| | 4 | 90.8(7) | 0.66(2) | 0 | 21(2) | $Hf_8Ni_{21}$ |
| | 5 | 49.9(5) | 0 | 0 | 18(2) | Hf |
| 673 | 1 | 29.2(6) | 0 | 0 | 31(2) | $HfNi_3^{(1)}$ |
| | 2 | 56(3) | 0 | 0 | 7(2) | $HfNi_3^{(2)}$ |
| | 3 | 64(1) | 0.38(6) | 0 | 17(2) | $Hf_2Ni_7$ |
| | 4 | 87.5(8) | 0.66(3) | 0 | 23(2) | $Hf_8Ni_{21}$ |
| | 5 | 49.6(7) | 0 | 0 | 22(2) | Hf |
| 773 | 1 | 28.2(6) | 0 | 0 | 32(2) | $HfNi_3^{(1)}$ |
| | 2 | 56.2(9) | 0 | 0 | 17(2) | $HfNi_3^{(2)}$ |
| | 3 | 62(1) | 0.31(7) | 0 | 19(2) | $Hf_2Ni_7$ |
| | 4 | 87(1) | 0.68(6) | 0 | 12(2) | $Hf_8Ni_{21}$ |
| | 5 | 49.5(5) | 0 | 0 | 19(2) | Hf |
| 873 | 1 | 28.6(6) | 0 | 0 | 33(2) | $HfNi_3^{(1)}$ |
| | 2 | 54(2) | 0 | 0 | 19(2) | $HfNi_3^{(2)}$ |
| | 3 | 61(1) | 0.34(6) | 0 | 17(2) | $Hf_2Ni_7$ |
| | 4 | 81(1) | 0.70(4) | 0 | 19(2) | $Hf_8Ni_{21}$ |
| | 5 | 49(1) | 0 | 0 | 13(2) | Hf |
| 973 | 1 | 28.2(4) | 0 | 0 | 31(2) | $HfNi_3^{(1)}$ |
| | 2 | 52.1(7) | 0 | 0 | 36(2) | $HfNi_3^{(2)}$ |
| | 3 | 59.9(3) | 0.31(2) | 0 | 27(2) | $Hf_2Ni_7$ |
| | 4 | 49(1) | 0 | 0 | 5(2) | Hf |
| 1073 | 1 | 28(1) | 0 | 0 | 39(2) | $HfNi_3^{(1)}$ |
| | 2 | 53(4) | 0 | 0 | 25(2) | $HfNi_3^{(2)}$ |
| | 3 | 58(1) | 0.47(9) | 0 | 27(2) | $Hf_2Ni_7$ |
| | 4 | 50(4) | 0 | 0 | 9(2) | Hf |
| 298† | 1 | 31.6(3) | 0 | 0 | 49(2) | $HfNi_3^{(1)}$ |
| | 2 | 70(2) | 0 | 0 | 10(2) | $HfNi_3^{(2)}$ |
| | 3 | 71(1) | 0.50(5) | 0 | 17(2) | $Hf_2Ni_7$ |
| | 4 | 51.9(7) | 0 | 0 | 23(2) | Hf |

† after measurement at 1073 K

Table 4: The parameters of the $\beta$-$HfNi_3$ and $ZrNi_3$ structure, given in $\mathring{A}$.

| | Our calculated results (WIEN 2k) [39, 44] | Experimental results (X-ray diffraction) [20, 25] | Earlier calculated results [45] |
|---|---|---|---|
| $HfNi_3$ | | | |
| $a$ | 5.285 | 5.2822(2) | 5.267 |
| $c$ | 21.419 | 21.3916(18) | 21.411 |
| $B$ [GPa] | 186 | | |
| Hf 2b | 0 0 1/4 | 0 0 1/4 | 0 0 1/4 |
| Hf2 4f | 1/3 2/3 0.3488 | 1/3 2/3 0.3488 | 1/3 2/3 0.3489 |
| Hf3 4f | 1/3 2/3 0.5458 | 1/3 2/3 0.5458 | 1/3 2/3 0.5461 |
| Ni 6h | 0.5110 0.022 1/4 | 0.5117 0.0234 1/4 | 0.5107 0.0213 1/4 |
| Ni2 12k | 0.156 0.312 0.0514 | 0.156 0.312 0.0514 | 0.1563 0.3126 0.0512 |
| Ni3 12k | 0.8320 0.6640 0.1495 | 0.8316 0.6632 0.1495 | 0.8322 0.6645 0.1496 |
| $ZrNi_3$ | | | |
| $a$ | 5.319 | 5.309 | 5.267 |
| $c$ | 4.305 | 4.303 | 21.411 |
| $B$ [GPa] | 177 | | |
| Zr 2c | 1/3 2/3 1/4 | 1/3 2/3 1/4 | 1/3 2/3 1/4 |
| Ni 6h | 0.8435 0.687 1/4 | 0.829 0.658 1/4 | 0.844291 0.688581 1/4 |

Table 5: The interatomic distances ($\mathring{A}$) less than 3.5 $\mathring{A}$ in $\beta$-$HfNi_3$.

| | Number of bonds | Interatomic distances measured from X-ray diffraction [25] | Interatomic distances calculated from the WIEN2k |
|---|---|---|---|
| Hf1 | | | |
| Hf1-Ni1 | 6 | 2.643(4) | 2.645 |
| Hf1-Ni3 | 6 | 2.644(4) | 2.648 |
| Hf2 | | | |
| Hf2-Ni3 | 6 | 2.642(3) | 2.643 |
| Hf2-Ni2 | 3 | 2.682(5) | 2.684 |
| Hf2-Ni1 | 3 | 2.670(2) | 2.673 |
| Hf3 | | | |
| Hf3-Ni2 | 3 | 2.638(5) | 2.640 |
| Hf3-Ni2 | 6 | 2.646(3) | 2.647 |
| Hf3-Ni3 | 3 | 2.684(5) | 2.686 |
| Ni1 | | | |
| Ni1-Ni1 | 2 | 2.455(1) | 2.457 |
| Ni1-Ni3 | 4 | 2.603(5) | 2.605 |
| Ni1-Hf1 | 2 | 2.643(4) | 2.645 |
| Ni1-Hf2 | 2 | 2.670(2) | 2.673 |
| Ni1-Ni1 | 2 | 2.827(1) | 2.828 |
| Ni2 | | | |
| Ni2-Ni2 | 2 | 2.471(8) | 2.474 |
| Ni2-Ni3 | 2 | 2.571(6) | 2.575 |
| Ni2-Ni2 | 2 | 2.623(8) | 2.624 |
| Ni2-Hf3 | 1 | 2.638(5) | 2.640 |
| Ni2-Hf3 | 2 | 2.646(3) | 2.647 |
| Ni2-Hf2 | 1 | 2.682(5) | 2.684 |
| Ni2-Ni2 | 2 | 2.812(8) | 2.812 |
| Ni3 | | | |
| Ni3-Ni2 | 2 | 2.571(6) | 2.575 |
| Ni3-Ni1 | 2 | 2.603(5) | 2.605 |
| Ni3-Ni3 | 2 | 2.616(8) | 2.615 |
| Ni3-Hf2 | 2 | 2.642(3) | 2.643 |
| Ni3-Hf1 | 1 | 2.644(4) | 2.648 |
| Ni3-Ni3 | 2 | 2.666(8) | 2.670 |
| Ni3-Hf3 | 1 | 2.684(5) | 2.686 |

Table 6: Calculated EFG values for $HfNi_3$ in units of $10^{21}$ V/m$^2$ and asymmetry parameters

| Probe | Lattice Site | EFG | asymmetry parameter ($\eta$) |
|---|---|---|---|
| no probe | Hf1 2b 0 0 1/4 | -1.3 | 0 |
| (pure compound) | Hf2 4f 1/3 2/3 0.3488(2) | -5.0 | 0 |
| | Hf3 4f 1/3 2/3 0.5458(1) | -2.2 | 0 |
| $^{181}$Ta | Hf1 2b 0 0 1/4 | -1.7 | 0 |
| | Hf2 4f 1/3 2/3 0.3488(2) | -7.1 | 0 |
| | Hf3 4f 1/3 2/3 0.5458(1) | -3.5 | 0 |